GEOPHYSICS, VOL. 71, NO. 5 (SEPTEMBER-OCTOBER 2006); P. P41–P51, 16 FIGS.
10.1190/1.2242449

3D volumetric multispectral estimates of reflector curvature and rotation

Saleh Al-Dossary[1] and Kurt J. Marfurt[2]

ABSTRACT

One of the most accepted geologic models is the relation between reflector curvature and the presence of open and closed fractures. Such fractures, as well as other small discontinuities, are relatively small and below the imaging range of conventional seismic data. Depending on the tectonic regime, structural geologists link open fractures to either Gaussian curvature or to curvature in the dip or strike directions. Reflector curvature is fractal in nature, with different tectonic and lithologic effects being illuminated at the 50-m and 1000-m scales. Until now, such curvature estimates have been limited to the analysis of picked horizons. We have developed what we feel to be the first volumetric spectral estimates of reflector curvature. We find that the most positive and negative curvatures are the most valuable in the conventional mapping of lineations — including faults, folds, and flexures. Curvature is mathematically independent of, and interpretatively complementary to, the well-established coherence geometric attribute. We find the long spectral wavelength curvature estimates to be of particular value in extracting subtle, broad features in the seismic data such as folds, flexures, collapse features, fault drags, and under- and overmigrated fault terminations. We illustrate the value of these spectral curvature estimates and compare them to other attributes through application to two land data sets — a salt dome from the onshore Louisiana Gulf Coast and a fractured/karsted data volume from Fort Worth basin of North Texas.

INTRODUCTION

The seismic expression of structural and stratigraphic discontinuities such as faults and channels may include lateral variation in waveform, dip, and amplitude. Estimates of seismic coherence (e.g., Bahorich and Farmer, 1995; Marfurt et al., 1998; Gerstzenkorn and Marfurt, 1999; Marfurt and Kirlin, 2000) provide a quantitative measure of the changes in waveform across a discontinuity. Estimates of apparent dip (e.g., Dalley et al., 1989; Barnes, 2000; Marfurt et al., 1998; Marfurt and Kirlin, 2000; Marfurt, 2006) provide a measure of change in reflector dip magnitude and azimuth across a discontinuity. Additionally, estimates of amplitude or coherent energy-weighted amplitude gradients (e.g., Luo et al., 1996, 2003; Marfurt and Kirlin, 2000; Marfurt, 2006) provide a measure of change in reflector amplitude across a discontinuity. Such discontinuity measures can highlight the boundaries between fault blocks, stratigraphic units, diagenetic alteration, and hydrocarbon accumulation.

One of the major goals of exploration seismology is the delineation of fractures. Fractures are found in nearly every reservoir, rock type, and depth; they may also be found in source rocks, reservoir rocks, and cap rocks. Petroleum explorationists pay a great deal of attention to locating these fractures to predict reservoir performance. Fractures can either advance or hinder our efforts in producing a reservoir. They may be confined to the reservoir or connect to deeper, water-bearing formations. Locating these fractures and identifying their orientations can help explorationists benefit from their presence or avoid their problems.

Using seismic coherence to detect fractures has been investigated since the first emergence of the coherence cube as a new attribute of seismic data. Skirius et al. (1999) used seismic coherence in carbonates in North America and the Arabian Gulf to detect faults and fractures. Luo et al. (2002) showed some examples from a Saudi Arabian carbonate field where amplitude gradients helped in delineating fractures. While coherence and amplitude gradients can often detect lineaments, reflector curvature is more directly linked to fracture distribution (Lisle, 1994; Roberts, 2001; Bergbauer et al., 2003). Hart et al. (2002) and Melville et al. (2004) have used horizon-based attributes (including various curvature attributes) to identify structural features that may be associated with fracture-swarm sweet spots. Hart and Sagan (2005) have used curvature to delineate stratigraphic features of interest. Stewart and Wynn (2000) pointed out that it may be necessary to examine curvature at various scales to account for different wavelengths, which was later initiated by Wynn and Stewart (2003) and Bergbauer et al. (2003) on interpreted horizons. While his paper also dealt with curvature computed from inter-

Manuscript received by the Editor February 23, 2004; revised manuscript received November 15, 2005; published online August 28, 2006.

[1] Saudi Aramco, PO Box 8851, Dhahran, Saudi Arabia. E-mail: saleh.dossary.6@aramco.com.
[2] Allied Geophysical Laboratories, University of Houston, Room 510-Science and Research Building 1, Cullen Road Entrance 14, Houston, Texas 77204. E-mail: kmarfurt@uh.edu.

preted horizons, Roberts (2001) anticipated that volumetric estimation of reflector curvature should be possible.

In the next section, we begin with a summary of alternative estimates of derivatives and show how we can use concepts presented by Cooper and Cowan (2003) as the building blocks for the multispectral curvature analysis discussed by Stewart and Wynn (2000). Next, we show how Roberts' (2001) measures of reflector curvature and independent measure of reflector rotation can be calculated directly from volumetric estimates of reflector dip (e.g., Marfurt, 2006; Barnes 2000). Finally, we apply these new attributes to data from onshore areas of Louisiana and Texas and show how long wavelength estimates of curvature enhance features that are difficult to see using either short wavelength estimates of curvature or coherence.

EVALUATION OF ALTERNATIVE DERIVATIVE CALCULATIONS

Luo et al. (1996) showed that lateral changes in reflector amplitude can be enhanced by a simple derivative, or Sobel filter that can be approximated by convolving the seismic data with the vector $[-1,0,+1]$. Clearly, if this simple approximation to the first derivative is valuable, we might assume that we can obtain superior results by replacing our three-sample, second-order accurate $[-1,0,+1]$ with a longer-length, higher-order accurate approximation of the first derivative. Alternatively, we may obtain better derivative-based edge detection by exploiting recent advances made in the 2D image processing literature (Torreao and Amaral, 2002) and applying them to 3D seismic data. A third alternative is to modify the fractional-order horizontal derivatives developed and applied to 2D potential field data by Cooper and Cowan (2003) and modify them to estimate 3D reflector curvature. Such fractional-order horizontal derivatives should allow us to analyze our data over a range of wavelengths and thereby delineate different scale features from the same time slice of 3D seismic data.

In this paper, our primary focus is on estimating curvature, rather than edge detection. Fortunately, even when viewed on time slices, vector dip is relatively slowly varying when compared to seismic amplitude. In fact, the lateral variability of vector dip is closer to that seen in photographic images and potential field data rather than that seen on seismic amplitude time slices. In the following sections, we summarize the theory and present the spectral response of each of our three alternate approaches.

Higher-order approximation to the first derivative

Higher-order accuracy approximations to derivatives are routinely used in numerical modeling of geophysical phenomena (e.g., Fornberg, 1987). What is not intuitively obvious is that we can interpret these approximations as an exact derivative multiplied by a low-pass filter. It is this low-pass filter framework of the exact derivative that will allow us to compare and evaluate the three seemingly disparate edge-detection algorithms described in these sections. As an illustration of the higher-order approximation of the first derivative, we derive a fourth-order-accurate derivative by expanding a function $u(x \pm h)$ and $u(x \pm 2h)$ where h is the separation between traces in a Taylor series

$$u(x+h) = u(x) + h\frac{d}{dx}u(x) + \frac{h^2}{2!}\frac{d^2}{dx^2}u(x) + \frac{h^3}{3!}\frac{d^3}{dx^3}u(x) + \frac{h^4}{4!}\frac{d^4}{dx^4}u(x) + O(h^5), \tag{1}$$

$$u(x-h) = u(x) - h\frac{d}{dx}u(x) + \frac{h^2}{2!}\frac{d^2}{dx^2}u(x) - \frac{h^3}{3!}\frac{d^3}{dx^3}u(x) + \frac{h^4}{4!}\frac{d^4}{dx^4}u(x) - O(h^5), \tag{2}$$

$$u(x+2h) = u(x) + 2h\frac{d}{dx}u(x) + \frac{(2h)^2}{2!}\frac{d^2}{dx^2}u(x) + \frac{(2h)^3}{3!}\frac{d^3}{dx^2}u(x) + \frac{(2h)^4}{4!}\frac{d^4}{dx^4}u(x) + O(h^5), \tag{3}$$

and

$$u(x-2h) = u(x) - 2h\frac{d}{dx}u(x) + \frac{(2h)^2}{2!}\frac{d^2}{dx^2}u(x) - \frac{(2h)^3}{3!}\frac{d^3}{dx^3}u(x) + \frac{(2h)^4}{4!}\frac{d^4}{dx^4}u(x) - O(h^5). \tag{4}$$

To obtain the first derivative du/dx, we multiply equations 1–4 by parameters a_1, a_2, a_3, and a_4, respectively, and sum them to obtain

$$a_1u(x+h) + a_2u(x-h) + a_3u(x+2h) + a_4u(x-2h) = (a_1+a_2+a_3+a_4)u(x) + e_1h\frac{d}{dx}u(x) + e_2h^2\frac{d^2}{dx^2}u(x) + e_3h^3\frac{d^3}{dx^3}u(x) + e_4h^4\frac{d^4}{dx^4}u(x), \tag{5}$$

where e_1, e_2, e_3 and e_4 are given by

$$\begin{aligned} e_1 &= a_1 - a_2 + 2a_3 - 2a_4, \\ e_2 &= \frac{1}{2}a_1 + \frac{1}{2}a_2 + 2a_3 + 2a_4, \\ e_3 &= \frac{1}{6}a_1 - \frac{1}{6}a_2 + \frac{4}{3}a_3 - \frac{4}{3}a_4, \\ e_4 &= \frac{1}{24}a_1 + \frac{1}{24}a_2 + \frac{2}{3}a_3 + \frac{2}{3}a_4. \end{aligned} \tag{6}$$

To express the first derivative only in terms of $u(x)$, $u(x \pm h)$, and $u(x \pm 2h)$, we need to choose the coefficients such that $e_2 = e_3 = e_4 = 0$ and $e_1 = 1$. Doing so gives $a_1 = +2/3$, $a_2 = -2/3$, $a_3 = +1/12$, and $a_4 = -1/12$, which, when inserted into equation 5, provides an approximation of the first derivative that is fourth-order accurate:

$$\frac{du(x)}{dx} = \frac{\frac{2}{3}u(x+h) - \frac{2}{3}u(x-h) - \frac{1}{12}u(x+2h) + \frac{1}{12}u(x-2h)}{h}. \tag{7}$$

Fornberg (1987) has carried these approximations out for a complete suite of higher-order-accurate operators (Figure 1). In the limit, the first-order derivative is approximated by

$$\frac{du}{dx} = F^{-1}\{ik_x F[u(x)]\}, \tag{8}$$

where F and F^{-1} denote the forward and inverse Fourier transforms, k_x is the wavenumber, and $i \equiv \sqrt{-1}$. In this paper, we interpret Figure 1 as a suite of low-pass filters applied to the exact derivative operator. Later, in Figure 11, we will show that filtered derivatives that enhance the longer wavelength variation of reflector dip provide images of subtle warping that were previously seen only on manually interpreted surfaces.

Torreao and Amaral's edge detector

Torreao and Amaral (2002) were not interested in curvature at all, but rather developed a robust edge detector that has derivative-like properties. They noticed that on many image-processing applications, they wanted to detect edges that segment different regions of smoothly varying signals contaminated by rapidly varying noise. They therefore chose to estimate signals that had the behavior

$$\bar{u}(x+L) = u(x) + O(x)^2 \tag{9}$$

for all values of x, where $u(x+L)$ is equal to the signal at location $x+L$. Using a Taylor series expansion, they rewrite equation 9 as

$$\bar{u}(x) + \frac{L}{1!}\frac{\partial \bar{u}}{\partial x} + \frac{L}{2!}\frac{\partial^2 \bar{u}}{\partial x^2} = u(x). \tag{10}$$

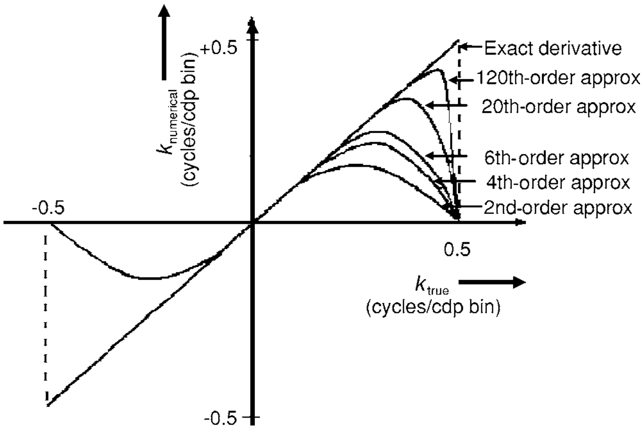

Figure 1. Spectral response of finite-difference approximations to the first derivative on a discrete grid, with grid increment h. Ideally, the numerical wavenumber $k_{\text{numerical}}$ should equal the true wavenumber k_{true}. The three-point, second-order accurate (Sobel filter) algorithm approximates the true wavenumber at low values of k_{true}. We can improve the accuracy of the first-derivative calculation by using higher-order approximations (and adding more points in the computation). Such higher-order approximations increase the high frequency content of the result (after Fornberg, 1987).

The Green's function solution corresponding to equation 10 is

$$G_2(+x) = \begin{cases} 0 & x < 0 \\ \frac{2}{L}\sin\left(\frac{x}{L}\right)\exp\left(-\frac{x}{L}\right) & x > 0 \end{cases}. \tag{11}$$

Next, they modify equation 10 to solve for the signal at x-L. If the signal is smoothly varying, these limits should be identical. They therefore form a difference operator

$$D_2(x) = \frac{1}{2L}[G_2(-x) - G_2(+x)]. \tag{12}$$

Note that in equation 12, we use the symbol D_2 rather than $\partial u/\partial x$. According to equation 10, $D_2(x) \equiv 0$ for both linear and parabolic signal variation. For information about a higher-order D_3 operator and a hybrid D_{23} operator by combining D_2 and D_3 operators, we refer the reader to Torreao and Amaral (2002), who find that the D_{23} operator is a better edge-detector operator.

We show the frequency response of Torreao and Amaral's (2002) D_{23} operator in Figure 2 for values of $L = h$, $2h$, $3h$, $4h$, and $5h$, where h is the separation between seismic traces. We note that the operator for $L = h$ is indistinguishable from the second-order finite-difference operator shown in Figure 1. Increasing the value of L increases both the number of seismic traces and the low-wavenumber (long-wavelength) spectral response of the operator. We have found Torreao and Amaral's (2002) D_{23} operator to be the most effective of the plethora of recently developed image-processing edge detectors when applied to seismic data. In particular, it produces more robust edges and curvature estimates than the classic derivatives shown in Figure 1. We were, however, troubled by the bimodal spectral response seen at values of $L = 4h$ and $L = 5h$ in Figure 2. Furthermore, the steep low-frequency slope of the spectra points bears a similarity to the fractional derivatives presented by Cooper and Cowan (2003).

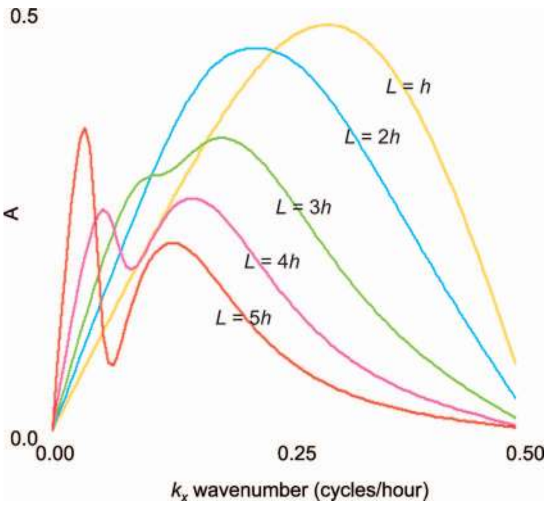

Figure 2. Spectral response of Torreao and Amaral's (2002) D_{23} edge detector for values of $L = h, 2h, 3h, 4h$, and $5h$. The $L = 2h$ operator has similar spectral content as the Sobel filter (second-order-accurate algorithm) shown in Figure 1.

Fractional-order derivatives

Cooper and Cowan (2003) applied fractional-order derivatives to gravity and magnetic data, thereby delineating linear features that are wavelength dependent. To show the mathematics behind the fractional derivative, let us assume that we have a function $u(x)$ and first derivative $\partial u/\partial x$. In the wavenumber domain, the first derivative is given by

$$F(\partial u/\partial x) = -\,\mathrm{i}k_x F[u(x)]. \tag{13}$$

We can therefore define the fractional horizontal derivative in the wavenumber domain as

$$F_\alpha(\partial u/\partial x) = (-\,\mathrm{i}k_x)^\alpha F[u(x)], \tag{14}$$

where α is a fractional real number.

Cooper and Cowan (2003) do not present implementation details. While a fractional derivative may be represented formally as $(\mathrm{i}k_\mathrm{x})^\alpha$ $\mathrm{F}(k_\mathrm{x})$, we have found it to be more useful to keep the phase change at a constant value of i, or 90°. In our implementation, we retain the amplitude spectrum weighting of the fractional derivative but keep the phase spectrum to be that of the conventional first derivative. Furthermore, building on experience in analyzing the efficacy of the Torreao and Amaral (2002) algorithm, we high-cut each filter by applying a simple raised cosine taper, $T(k_x)$. The peak of the raised cosine taper is at $\alpha k_{\mathrm{Nyquist}}/2$, where $k_{\mathrm{Nyquist}} = 1/(2h)$. Finally, for scaling purposes, we find it useful to normalize the energy of each filter to a constant that is equal to the energy of the filter associated with $\alpha = 1.0$ (Figure 3). Our derivative operator D_x can thus be expressed as

$$D_x = F^1\{-\,\mathrm{i}(k_x)^\alpha \mathrm{F}[u(x)]T(k_x)\}. \tag{15}$$

In this manner, our approximation of D_x for $\alpha = 1.0$ is identical to that of the second-order finite-difference operator and Torreao and Amaral's (2002) D_{23} operator with $L = h$.

Summarizing the previous discussion, we note that:

1) Increasing the accuracy of a numerical estimate of a derivative computed on a discrete grid requires a larger analysis window (more points in the computation). The major impact of such a computation is to increase the short-wavelength components of the results (Figure 1).
2) Sophisticated edge detectors developed by the image-processing community, represented by Torreao and Amaral's (2002) D_{23} operator, improve over conventional derivative operators such as the Sobel filter by increasing the long-wavelength with respect to the short-wavelength components of the image (Figure 2).
3) We can derive a simpler long-wavelength-enhanced derivative operator by low-pass filtering the results of a conventional first-derivative operator (Figure 3). By doing so, we retain the visual advantages of Torreao and Amaral's (2002) D_{23} operator, while producing images that can be directly interpreted as band-passed estimates of reflector shape.

ALTERNATIVE MEASURES OF REFLECTOR SHAPE

Seismic reflectors are rarely planar but are usually folded or even broken. Many regions of the earth's subsurface can best be described as chaotic. Most published work in mapping reflector shape has been restricted to represent interpreted horizons by their curvature (Lisle, 1994; Stewart and Wynn, 2000; Roberts, 2001; Sigismondi and Soldo, 2003). This work in turn has been based on a great deal of literature on mapping surface topography or terrain (e.g., Mitsova and Hofierka, 1993; Wood, 1996). In this paper, we wish to develop an algorithm that estimates reflector shape on a complete cube of seismic data without the need for prior interpretation. While assigning a picked reflector surface to each point in a given seismic data volume proves intractable, assigning a vector dip (or alternative dip magnitude and dip azimuth) is not. Barnes (1996, 2000) shows how to calculate reflector dip and azimuth using a 3D generalization of instantaneous frequency. Instantaneous frequency ω (and wavenumbers k_x and k_y) estimates suffer from waveform interference, so considerable smoothing needs to be done to stabilize the calculation. We have found that an estimate of reflector dip based on a multiwindow co-

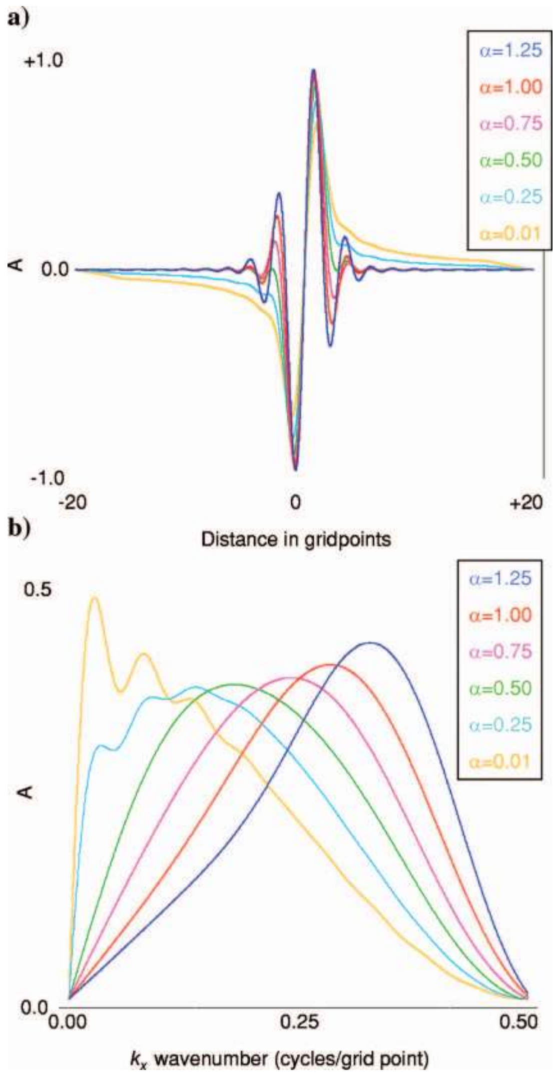

Figure 3. (a) Spatial operators and (b) their corresponding spectra used in the fractional derivative D_α, given by equation 14. By design, our first-order derivative ($\alpha = 1.00$) has similar spectral content as the second-order accurate finite-difference operator (Sobel filter) shown in Figure 1 and Torreao and Amaral's (2002) filter, shown in Figure 2. As we decrease the value of α, we also decrease the higher frequencies, thereby shifting the bandwidth toward the longer wavelengths (lower values of k_x).

herence scan (Marfurt, 2006) produces both stable and high lateral resolution results. The examples shown in this paper will use this latter technique as input; however, we have found that long-wavelength (low-wavenumber) estimates of reflector shape using envelope-weighted estimates of instantaneous dip and azimuth (Barnes, 2000) as input also produce good results.

Given a cube of estimated vector dip

$$u(z,x,y) = p(z,x,y)\hat{\mathbf{x}} + q(z,x,zy)\hat{\mathbf{y}}, \qquad (16)$$

where p and q are the components of dip and where $\hat{\mathbf{x}}$ and $\hat{\mathbf{y}}$ are unit vectors along the Cartesian axes, we can mathematically decompose them into two parts:

$$\mathrm{div}(\mathbf{u}) = (\partial p/\partial x + \partial q/\partial y) \qquad (17)$$

and

$$r_z = (\partial p/\partial y - \partial q/\partial x). \qquad (18)$$

In principal, any arbitrary vector field can be expressed by some linear combination of equations 17 and 18. Equation 17 is the divergence of the vector dip, which for the case $p = q = 0$ at the analysis point, is proportional to Roberts' (2001) definition of mean curvature, k_{mean}. Equation 18, which we will say the reflector rotation r_z is the vertical component of the curl of the vector dip. The vertical component of curl $(\mathbf{u})$ is nonzero when the dip estimates are noisy or when there is a strike/slip component of deformation. The other components of the rotation vector correspond to acquisition rather than (approximately) depositional axes; we have not found them to be particularly useful. Other than some preliminary work by Marfurt and Kirlin (2000), we have not seen any published literature using this measurement on interpreted surfaces.

In contrast, there is a great deal of relevant literature published on the use of curvature. Following the notation of Roberts (2001), we can represent a reflector surface $z(x,y)$ by a quadratic surface:

$$z(x,y) = \alpha x^2 + by^2 + cxy + dx + ey + f. \qquad (19)$$

A fixed depth (or time) slice through this surface will be

$$\text{an ellipse, if } c^2 - 4ab > 0, \qquad (20)$$

$$\text{a hyperbola, if } c^2 - 4ab < 0, \qquad (21)$$

or

$$\text{a parabola, if } c^2 - 4ab = 0. \qquad (22)$$

Using our input estimates of reflector dip, p and q, the coefficients in equation 19 become at $x = y = 0$:

$$D_x(D_x z) = 2a = D_x p,$$

$$D_y(D_y z) = 2b = D_y q,$$

$$D_x q + D_y p = 2c,$$

and

$$e = q, \qquad (23)$$

where the operators D_x and D_y can be any of the numerical approximations to the first derivative that was discussed in the previous section. We should note that by construction, equation 19 does not express any rotational component, since

$$r_z = D_y D_x z - D_x D_y z = c - c = 0. \qquad (24)$$

When the coefficient c in equation 19 is nonzero, the quadratic surface $z(x,y)$ is said to be rotated with respect to its principal axes. To find the maximum and minimum (or principal) curvatures k_{min} and k_{max}, we need to rotate the coordinate system to another frame. Details can be found in Roberts (2001) as well as in advanced mathematics books on solid geometry and 3D computer graphics. We will use the terminology (and equations) presented by Roberts (2001) and calculate the mean curvature k_{mean},

$$k_{\mathrm{mean}} = [a(1 + e^2) + b(1 + d^2) - cde]/(1 + d^2 + e^2)^{1/2}; \qquad (25)$$

the Gaussian curvature k_{Gauss},

$$k_{\mathrm{Gauss}} = (4ab - c^2)/(1 + d^2 + e^2)^2; \qquad (26)$$

the maximum and minimum curvatures k_{max} and k_{min},

$$k_{\mathrm{max}} = k_{\mathrm{mean}} + (k_{\mathrm{mean}}^2 - k_{\mathrm{Gauss}})^{1/2}, \qquad (27a)$$

$$k_{\mathrm{min}} = k_{\mathrm{mean}} - (k_{\mathrm{mean}}^2 - k_{\mathrm{Gauss}})^{1/2}; \qquad (27b)$$

the most positive curvature k_{pos},

$$k_{\mathrm{pos}} = (a + b) + [(a - b)^2 + c^2]^{1/2}; \qquad (28)$$

the most negative curvature k_{neg},

$$k_{\mathrm{neg}} = (a + b) - [(a - b)^2 + c^2]^{1/2}; \qquad (29)$$

the dip curvature,

$$k_{\mathrm{dip}} = 2(ad^2 + be^2 + cde)/[(d^2 + e^2)(1 + d^2 + e^2)^{3/2}]; \qquad (30)$$

the strike curvature k_{strike}

$$k_{\mathrm{strike}} = 2(ae^2 + bd^2 - cde)/[(d^2 + e^2)(1 + d^2 + e^2)^{1/2}]; \qquad (31)$$

the curvature C,

$$C = [(k_{\mathrm{max}}^2 + k_{\mathrm{min}}^2)/2]^{1/2}; \qquad (32)$$

the shape index s,

$$s = \frac{2}{\pi} \tan^{-1}\left[\frac{k_{\mathrm{min}} + k_{\mathrm{max}}}{k_{\mathrm{min}} - k_{\mathrm{max}}}\right]; \qquad (33)$$

and finally, the azimuth of the maximum curvature ψ,

$$\psi = \begin{cases} \tan^{-1}[c/(a - b)] & \text{if } a \neq b \\ \pi/4 & \text{if } a = b \end{cases}. \qquad (34)$$

The maximum and minimum (also called principal curvatures) k_{max} and k_{min} measure the maximum and minimum bending of the surface at each point (Lisle, 1994). Sigismundi and Soldo (2003) show that the maximum curvature allows one to easily determine the relative movement of fault blocks from time slices. In Figure 4, we show reflector shapes as a function of the sign of the most positive and most negative curvature. The Gaussian curvature k_{Gauss} is positive for bowls and domes, negative for hyperboloids and zero for planes everywhere. The Gaussian curvature k_{Gauss}, sometimes referred to as the total curvature, is named after Gauss and his Theorema Egregium or "wonderful theory" (Roberts, 2001). Lisle (1994) suggested Gaussian curvature as a method of predicting fractures. Robert (2001) found Gaussian curvature to be a poor delimiter of faults because faults are generally expressed as linear features on attribute maps. Linear features tend to have values of $k_{\min}$ that fluctuate around zero. Consequentially, k_{Gauss} will also be zero. We will show later in Figures 13c and 14c that k_{Gauss} is a good estimate of elliptical-shaped collapse features.

We find the most positive and most negative curvatures k_{pos} and k_{neg} to be the most useful in delineating faults, fractures, flexures, and folds. These two measures consistently show the same polarity for a given geologic feature, allowing one to better track it, either visually or with computer software. Furthermore, a simple dual gradational color bar allows us to interpret negative values of most positive curvature as bowls and postive values of most negative curvature as domes (Figure 4). We find the "reflector rotation" attribute, r_z, to be more sensitive to acquisition footprint than other reflector shape measures (at least for land data where there is a strong azimuthal and offset bias on output lines). At present, we use reflector rotation primarily as a measure of the quality of our input dip and azimuth estimates. We expect that there are more robust expressions of "tears" in the reflector surface; however, we leave this analysis for future work.

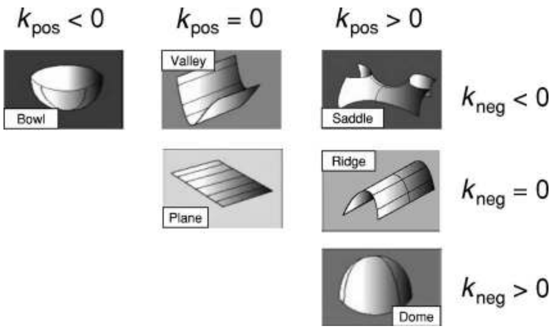

Figure 4. Classification of quadratic shapes based on most negative and most positive curvature (modified from Bergbauer et al., 2003).

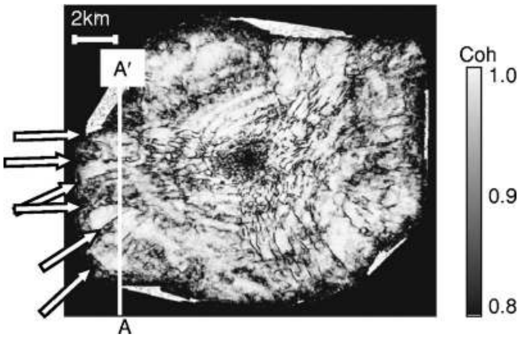

Figure 5. Principal component coherence through a survey acquired over Vinton Dome, Louisiana, USA. The arrows correspond to the faults shown in Figures 6–8. Data courtesy of OPEX.

APPLICATION

To illustrate the value of our method, we calculate curvature and rotation attributes for two data sets — a salt dome from the onshore Louisiana Gulf Coast and a fractured/karsted data volume from the Fort Worth basin of North Texas. We begin by comparing a suite of time slices through attribute cubes generated for Vinton Dome, Louisiana, at 1.0 s. As a baseline, we plot a time slice through the principal component coherence volume in Figure 5. Zones of low coherence correspond to lateral changes in waveform, rather than in changes of amplitude, dip, or curvature. We note that the faults seen in line AA′ in Figure 6 do not all show up on the coherence time slice at 1.0 s seen in Figure 5. In some places, the fault appears to have some drag. At other places, the reflector terminations appear to be incompletely focused.

In Figure 7, we display the most negative curvature, most positive curvature, and rotation images corresponding to the coherence image shown in Figure 5. We have calculated these images using a short-wavelength approximation of curvature using D_x and D_y corresponding to $\alpha = 1.00$. We judge the value of these images as poor, primarily because of the poor focusing of the prestack time migration used in imaging what we know to be a structurally complex area. In Figure 8 we show the corresponding long wavelength images calculated using a value of $\alpha = 0.25$. Here, the most positive and negative curvature time slices more clearly delineate the radial faults about the salt dome. Note that each of the faults indicated on Figure 8a and b are indicated on the vertical time slice in Figure 6. The rotation time slice in Figure 8c shows what we interpret to be faults with a rotation about them (white arrows). There is a lake over the crest of the salt dome, giving rise to low fold, poor data quality, and poor estimates of dip/azimuth at this time slice (black arrow), resulting in unreasonably large values of rotation r_z.

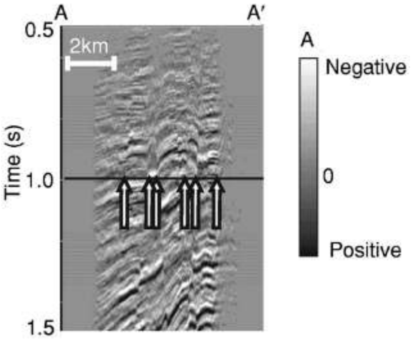

Figure 6. A vertical section through the seismic data corresponding to line AA′ shown in Figure 5. The arrows depict faults indicated by the arrows in Figures 5, 7, and 8. Note that some of these faults appear to be discrete discontinuities, while others appear to be folds, either from drag along the fault or from inaccurate migration. Faults having a folded appearance show up more clearly in the curvature volumes.

Next, we turn our attention to a time slice at t = 0.8 s through the Fort Worth basin survey that is roughly at the Caddo/Atoka horizon. In Figure 9 we display the coherence, while in Figure 10, we display line BB′ through the input seismic data volume, and note the collapse features that begin at the basement level (indicated by arrows). To better understand the spectral nature of our curvature estimates, we display a suite of negative curvature images k_{neg} in Figure 11 corresponding to values of $\alpha = 2.00$, 1,50, 1.00, 0.75, 0.50, and 0.25. We confirm Stewart and Wynn's (2000) observation that multispectral analysis brings out different features — highly localized faults and fracture swarms for larger values of α (Figure 11c) and more regional warping and flexures for smaller values of α (Figure 11f).

In Figure 12, we examine a deeper time slice at $t = 1.2$ s that cuts across the Ellenburger and Marble Falls Formations. Collapse features seen in Figure 10 cut both of these horizons (Sullivan et al., 2006) and appear as elliptical zones of lower coherence in Figure 12. We display the most negative, most positive, and Gaussian curvature time slices in Figures 13 and 14, calculated using values of $\alpha = 1.00$ and $\alpha = 0.25$. Most negative and most positive curvature measurements are independent of each other and in general provide mathematically uncorrelated images. Here we note that the lineaments seen in the shallower section in Figure 11f are more highly developed, indicating that collapse features are structurally controlled (Sullivan et al., 2006). The bowl-shaped collapse features themselves (as well as a few domal features) show up clearly on the

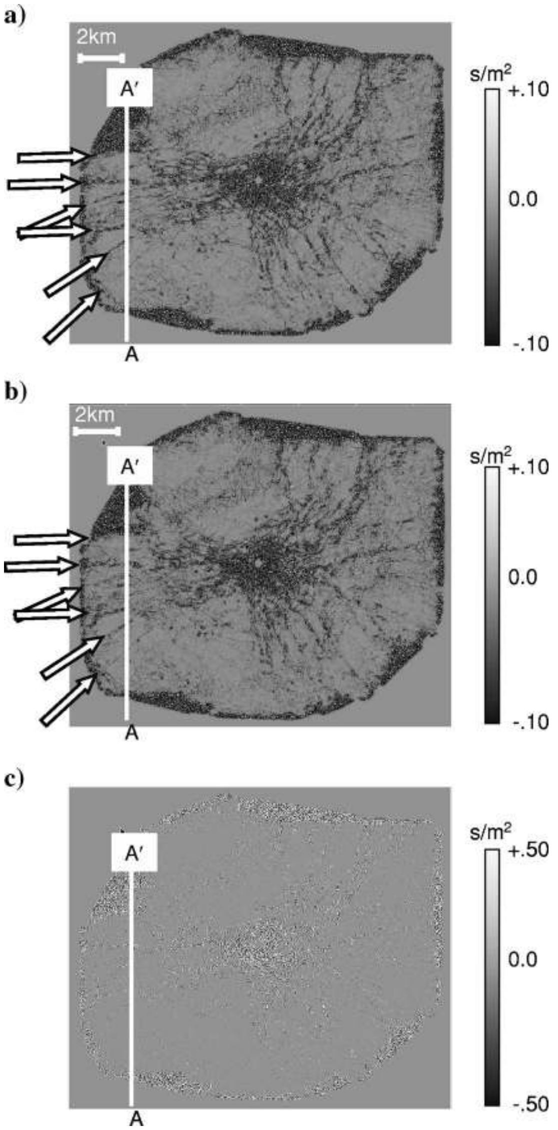

Figure 7. Short-wavelength ($\alpha = 1.00$) estimates of (a) most negative curvature k_{neg}, (b) most positive curvature k_{pos}, and (c) reflector rotation r_z, corresponding to the same time slice shown in Figure 5.

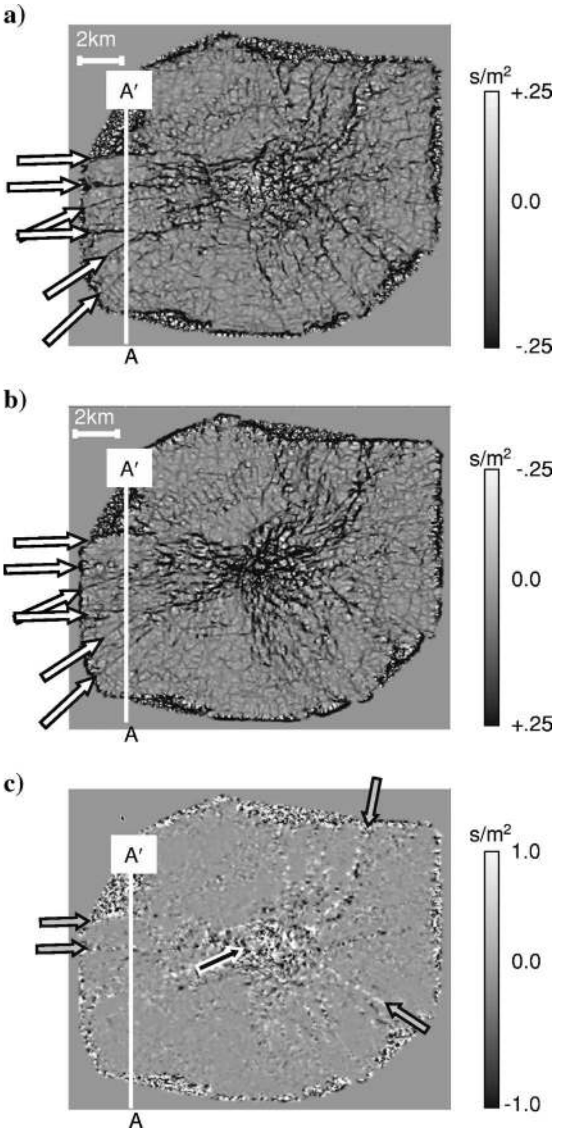

Figure 8. Long-wavelength ($\alpha = 0.25$) estimates of (a) most negative curvature k_{neg}, (b) most postive curvature k_{pos}, and (c) reflector rotation r_z, corresponding to the same time slice shown in Figures 5 and 7. White arrows depict faults that are not as clearly seen on the coherence time slice shown in Figure 5. Gray arrows correspond to faults where reflectors have significant rotation about the fault plane. Such rotations are not represented by the quadratic surface used in curvature calculations. The black arrow indicates noisy, low-fold areas of the data.

Gaussian curvature as positive-value white circles in Figures 13c and 14c. We do not see the lineations in the Gaussian curvature images. For completeness, we display the dip and strike curvature in Figure 15. In a compressional terrain, Hart et al. (2002) predict that large values of k_{strike} will be correlated to open versus closed fractures. In a tensional terrain such as the Austin Chalk (Schnerk and Madeen, 2000), others find that dip curvature correlates with open fractures (Mark Stevenson, Geotexture, personal communication). We leave the study of which curvature attributes best correlate to fractures and production in this Fort Worth basin survey for a future paper. Suffice it to say that these images are significantly different from each other and merit their own geostatistical analysis.

Finally in Figure 16, we display the shape index and curvature at both the $t = 0.8$ s and $t = 1.2$ s levels using a 2D color bar. We plot the shape index against hue and curvature against lightness, such that shapes having little or no curvedness appear to be black, indicating a planar shape. In the shallow time slice in Figure 16b, we note our channel in the northwest has a valley shape (in cyan). To the southeast we see a yellow ridge feature that corresponds to the black arrow in Figure 10. In the deeper time slice shown in Figure 16c, we can unambiguously see the collapse features (seen in blue and cyan). These collapse features are separated from each other by ridges (yellow) and saddles (green). There are only a few dome features (red) at this level.

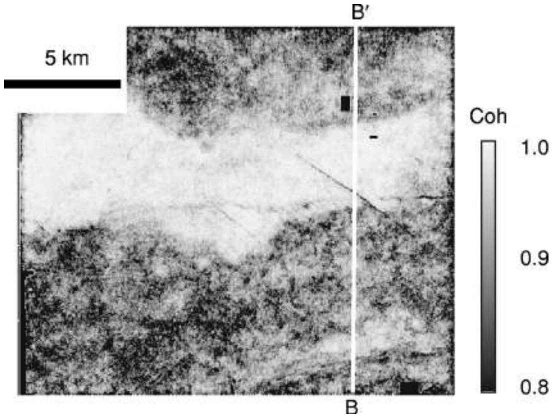

Figure 9. Principal component coherence at $t = 0.8$ s (approximately the Caddo/Atoka level) through a survey from the Fort Worth basin, Texas, USA. Data courtesy of Devon Energy.

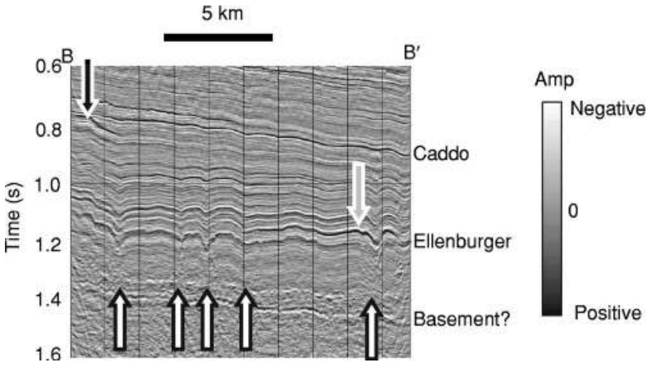

Figure 10. Line BB′ through the seismic data cube. White arrows indicate collapse features that appear to be basement controlled. Black arrow indicates a ridge that can be seen in Figure 16b. Gray arrow indicates a dome that can be seen on Figure 16c.

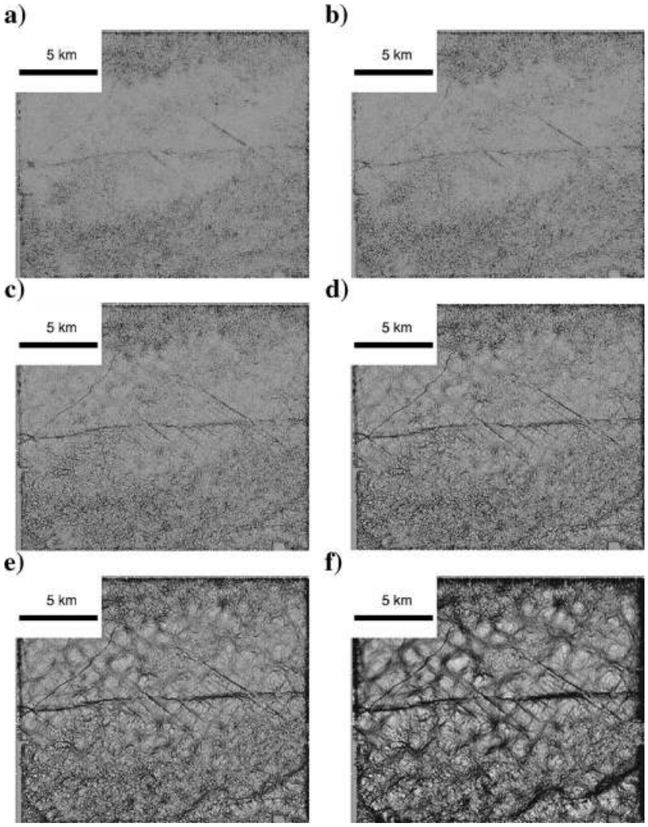

Figure 11. Time slice at $t = 0.8$ s corresponding to Figure 9, showing most negative curvature k_{neg}, computed using fractional derivatives with values of α = (a) 2.00, (b) 1.50, (c) 1.00, (d) 0.75, (e) 0.50, and (f) 0.25.

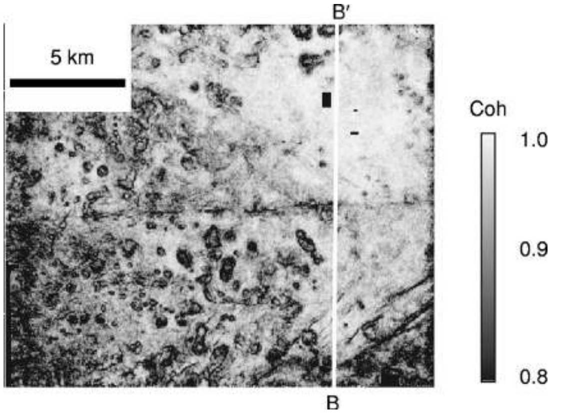

Figure 12. Principal component coherence at $t = 1.2$ s (approximately the Ellenburger level shown in Figure 10) through the same survey shown in Figure 9.

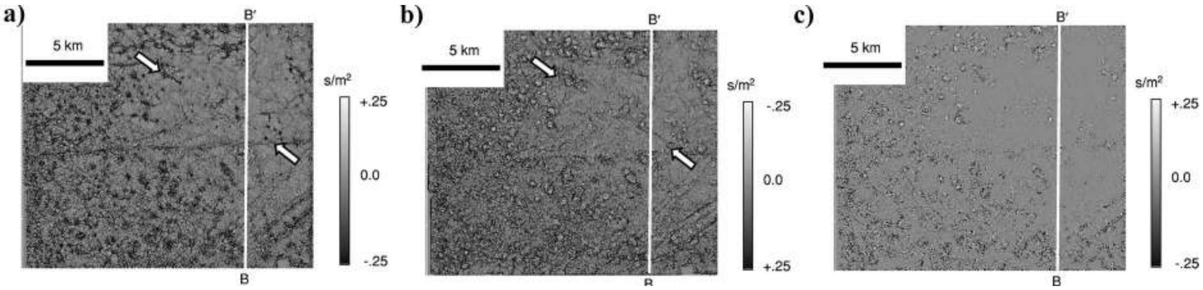

Figure 13. Short-wavelength ($\alpha = 1.00$) curvature values at $t = 1.2$ s corresponding to Figure 12 of (a) most negative curvature k_{neg}, (b) most positive curvature k_{pos}, and (c) Gaussian curvature k_{Gauss}. Arrows indicate elongated collapse feature that appears to be structurally controlled.

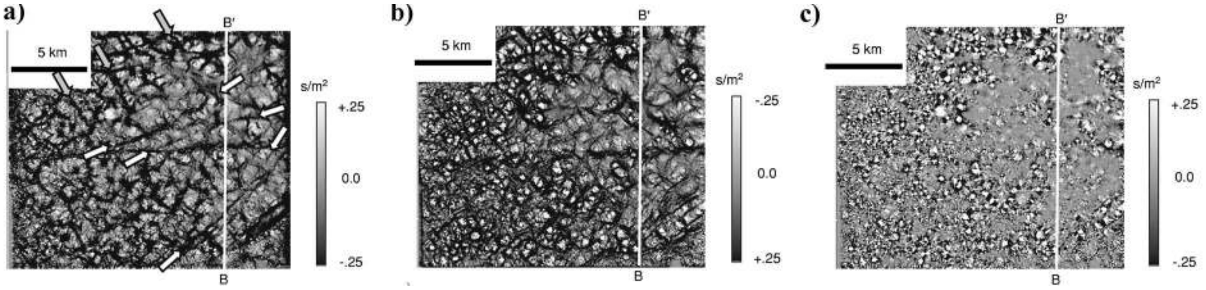

Figure 14. Long-wavelength ($\alpha = 0.25$) curvature values at $t = 1.2$ s corresponding to Figure 12 of (a) most negative curvature k_{neg}, (b) most positive curvature k_{pos}, and (c) Gaussian curvature k_{Gauss}. By examining Figure 4, we see that positive values of k_{neg} in (a) correspond to domes while negative values of k_{pos} in (b) correspond to bowls. White arrows indicate through-going northeast-southwest lineaments that appear to offset northwest-southeast lineaments indicated by gray arrows. These lineaments are much more clearly seen than in Figure 13.

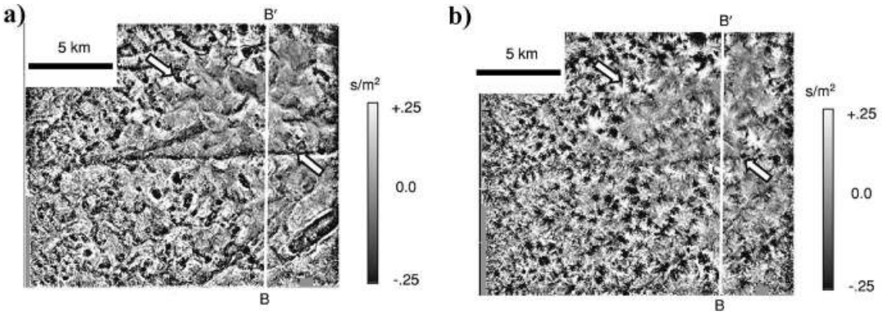

Figure 15. (a) Dip curvature k_{dip}, and (b) Strike curvature k_{strike}, corresponding to the time slices in Figure 14. While we find these images less useful than k_{neg} and k_{pos} in interpreting faults and flexures, Hart et al. (2002) and others, find these measures more closely correlated to open fractures.

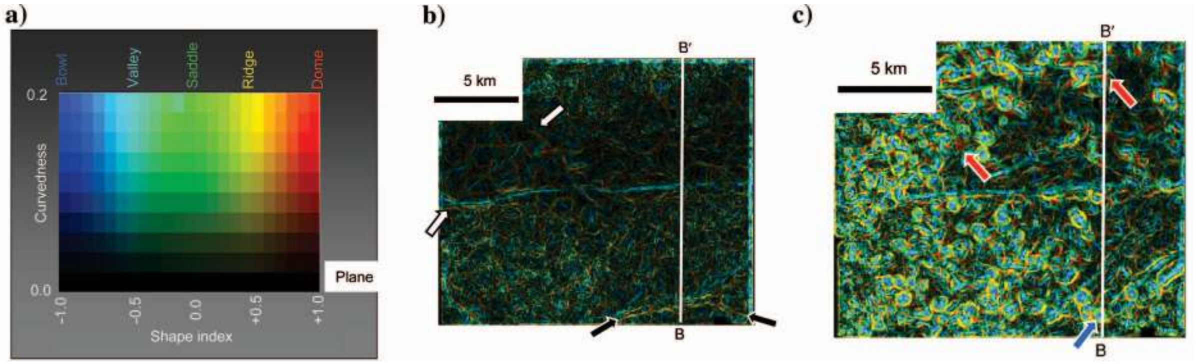

Figure 16. (a) A 2D color table used to display the shape index against curvature. Planar features will have a curvature near zero and will be displayed black. Highly curved features will be plotted as a pure color, allowing us to differentiate between reflector shapes. We plot curvature c, and shape index s, calculated using equations 32 and 33, using this 2D color table at (b) $t = 0.8$ s corresponding to Figures 9 and 11 and (c) $t = 1.2$ s corresponding to Figures 12–15. Note that the shallow section is less contorted, yielding a darker image. The cyan "valley" indicated by arrows in (b) corresponds to a channel. The yellow ridge indicated by the black arrow corresponds to the ridge seen in Figure 10. Other cyan valley and yellow ridge lineaments correspond to deformation about faults and joints. In contrast, (c) is dominated by collapse features in the Ellenburger Formation. Collapse features appear as blue circles, such as the one indicated by the blue arrow, ringed by yellow ridges and green saddles. Red arrows indicate two domal features, one of which corresponds to the dome indicated by the gray arrow seen in Figure 10.

CONCLUSIONS

We have developed a means by which powerful seismic attributes that could previously be applied only to interpreted horizons can now be applied to the entire uninterpreted volume of seismic data. These attributes, which include measures of reflector rotation and curvature, are independent of, and complementary to, the popular measures of seismic coherence. We find reflector rotation to be a good indicator of data quality as well as scissor movement along a fault. We find the most negative and most positive curvatures to be the most easily interpreted of the curvature images in highlighting faults and folds. In addition, domes will appear as positive anomalies on most negative curvature, while bowls will appear as negative anomalies on most positive curvature. Although the images may appear somewhat “busy,” the maximum curvature can allow one to visualize the direction of fault throw on a time slice. The Gaussian curvature shows what it was designed to show — surfaces that exhibit an elliptical bowl or dome component — and appears to be a good indicator of karst infill. Gaussian curvature, which is the product of the two principal curvatures, is not a good indicator of faults. Faults are typically curvilinear features for which one of the principal curvatures tends towards zero. The shape index, when corendered with curvedness, allows one to visualize 3D reflector morphology on simple time slices. In addition to highlighting lineations, structural geologists have theoretical and empirical evidence linking Gaussian, dip, and strike curvatures to fracture density. We are now able to make such predictions through a complete, uninterpreted data cube.

We agree with Stewart and Wynn (2000) that measurements of reflector shape, such as curvature and rotation, are fractal in nature, rendering them amenable to multispectral analysis such as shown in Figure 11. We have found that the long-wavelength estimates of curvature are particularly valuable in extracting information that was previously difficult or impossible to see. While we do indeed see individual large-scale joints and fractures (such as in Figures 11 and 14), we do not expect to visualize individual fractures below the limits of seismic resolution. Rather, our workflow would be to mimic Lisle’s (1994) outcrop work and statistically correlate subseismic resolution fractures measured on well logs and inferred through production data to curvature measurements seen at the seismic scale. This calibration effort is currently the major focus of our research.

Curvature and rotation (and other possible measures of reflector shape) are mathematically independent of coherence and seismic amplitude. The relationship between fractures and curvature is well established in the structural geology community. While we expect the impact of 3D volumetric estimates of reflector shape to be every bit as big as the impact of coherence on seismic interpretation, we also anticipate a good workflow to include all of these geometric attribute tools.

This work is in its infancy. Thus, we see a need to quantitatively calibrate the features seen in curvature and rotation to direct measures of fractures through both horizontal image logs and microseismicity epicenter location during frac tests. We also see a need to qualitatively calibrate these curvature and rotation features directly to production data.

If there is a major limitation to this technology, it is in the calculation itself. The vector dip is a true 3D calculation that follows the best reflector, which includes the analysis point. However, since we wish to calculate curvature even when there are only piecewise continuous reflectors available, we calculate the derivatives of dip on time slices. For steeply dipping horizons and long-wavelength estimates, we expect these measures will undesirably mix geology of different formations. Predictions of fracture intensity will no longer be linked to thin plate theory but rather to some more complicated composite plate deformation. While we anticipate near-term improvements in our estimates to better follow the local dip, we know such improvements will not be trivial to implement.

ACKNOWLEDGMENTS

The authors wish to acknowledge and thank the U. S. Department of Energy for their support during the period during which this work was performed as part of grant DE-FC26-01BC15353, focused on the geophysical analysis of Vinton Dome, Louisiana. Other studies were supported by the sponsors of Allied Geophysical Laboratories and by the Advanced Technical Program of the State of Texas. We thank OPEX and Devon Energy for their geologic insight and for permission to use their 3D seismic data. We also thank our geological colleagues at Allied Geophysical Laboratories — Peter Bartok, Chuck Blumentritt, Al Lacazette, Isabel Serrano, and Charlotte Sullivan — for their enthusiasm, encouragement, and tutelage on the use of curvature in structural interpretation.

S. Al-Dossary wishes to thank Saudi Aramco for the opportunity and support in pursuing his graduate studies and, in particular, Yi Luo for his encouragement and support in pursuing this research.

REFERENCES

Bahorich, M. S., and S. L. Farmer, 1995, 3-D seismic discontinuity for faults and stratigraphic features, The coherence cube: The Leading Edge, **16**, 1053–1058.

Barnes, A. E., 1996, Theory of 2D complex seismic trace analysis: Geophysics, **61**, 264–272.

——, 2000, Weighted average seismic attributes: Geophysics, **65**, 275–285.

Bergbauer, S., T. Mukerji, and P. Hennings, 2003, Improving curvature analyses of deformed horizons using scale-dependent filtering techniques: AAPG Bulletin, **87**, 1255–1272.

Cooper, G. R. J., and D. R. Cowan, 2003, The meter reader — Sunshading geophysical data using fractional order horizontal gradients: The Leading Edge, **22**, 204–205.

Dalley, R. M., E. E. A. Gevers, G. M. Stampli, D. J. Davies, C. N. Gastaldi, P. R. Ruijetnberg, and G. J. D. Vermeer, 1989, Dip and azimuth displays for 3-D seismic interpretation: First Break, 7, 86–95.

Fornberg, B., 1987, The pseudospectral method: Comparisons with finite differences for the elastic wave equation: Geophysics, **52**, 483–501.

Gersztenkorn, A., and K. J. Marfurt, 1999, Eigenstructure based coherence computations: Geophysics, **64**, 1468–1479.

Hart, B. S., R. A. Pearson, and G. C. Rawling, 2002, 3-D Seismic horizon-based approaches to fracture-swarm sweet spot definition in tight-gas reservoirs: The Leading Edge, **21**, 28–35.

Hart, B. S., and J. A. Sagan, 2005, Curvature helps strat interpretation: AAPG Geologists Explorer, no., 2, www.aapg.org/explorer/geophysical_corner/2005/02gpc.cfm, Accessed November, 15, 2005.

Lisle, R. J., 1994, Detection of zones of abnormal strains in structures using Gaussian curvature analysis: AAPG Bulletin, **78**, 1811–1819.

Luo, Y., S. Al-Dossary, M. Marhoon, and M. Alfaraj, 2003, Generalized Hilbert transform and its application in Geophysics: The Leading Edge, **22**, 198–202.

Luo, Y., W. G. Higgs, and W. S. Kowalik, 1996, Edge detection and stratigraphic analysis using 3D seismic data: 66th Annual International Meeting, Society of Exploration Geophysicists, Expanded Abstracts, 324–327.

Luo, Y., M. Marhoon, S. Al-Dossary, and M. Alfaraj, 2002, Edge-preserving smoothing and applications: The Leading Edge, **21**, 136–158.

Marfurt, K. J., 2006, Robust estimates of 3D reflector dip: Geophysics, 71, this issue.

Marfurt, K. J., and R. L. Kirlin, 2000, 3-D broad-band estimates of reflector dip and amplitude: Geophysics, **65**, 304–320.

Marfurt, K. J., R. L. Kirlin, S. L. Farmer, and M. S. Bahorich, 1998, 3-D seismic attributes using a semblance-based coherency algorithm: Geophysics, **63**, 1150–1165.

Melville, P., O. al Jeelani, S. al Menhali, and J. Grotsch, 2004, Three-dimensional seismic analysis in the characterization of a giant carbonate field, onshore Abu Dhabi, United Arab Emirates, *in* G. P. Eberli, J. L. Masaferro, and J. F. Sarg, eds., Seismic imaging of carbonate reservoirs and systems: AAPG Memoir, **81**, 123–148.

Mitasova, H., and J. Hofierka, 1993, Interpolation by regionalized spline with tension: II. Application to terrain modeling and surface geometry analysis: Mathematical Geology, **25**, 657–669.

Roberts, A., 2001, Curvature attributes and their application to 3D interpreted horizons: First Break, 19, 85–99.

Schnerk, G. C., and C. N. Madeen, 2000, The Austin Chalk: Simulation of horizontal wells in a heterogeneous formation: Society of Petroleum Engineers, SPE 20716.

Sigismondi, E. M., and C. J. Soldo, 2003, Curvature attributes and seismic interpretation: Case studies from Argentina basins: The Leading Edge, **22**, 1122–1126.

Skirius, C., et al., 1999, 3-D seismic attributes applied to carbonates: The Leading Edge, **18**, 384–389.

Stewart, S. A., and T. J. Wynn, 2000, Mapping spatial variation in rock properties in relationship to scale-dependent structure using spectral curvature. Geology: **28**, 691–694.

Sullivan, E. C., K. J. Marfurt, A. Lacazette, and M. Ammerman, 2006, Application of new seismic attributes to collapse chimneys in the Fort Worth Basin: Geophysics, 71, this issue.

Torreao, J. R. A., and M. S. Amaral, 2002, Signal differentiation through a Green's function approach: Pattern Recognition Letters, **23**, 1755–1759.

Wood, J. D., 1996, The geomorphological characterization of digital elevation models: Ph.D. thesis, University of Leicester.

Wynn, T. J., and S. A. Stewart, 2003, The role of spectral curvature mapping characterizing subsurface strain distributions, *in* M. Ameen, ed., Fractures and in-situ stress characterization of hydrocarbon reservoirs: Geological Society Special Publication 209, 127–143.